

Supplementary Material for Bilyard *et al.* 'High-resolution characterization of the enzymatic states in *E. coli* F₁-ATPase'

E. coli F₁-ATPase

The *E. coli* F₁F₀ plasmid pBUR17AH10GC2 with ten histidine residues introduced into the α -subunit amino terminus was constructed from pBUR17- γ 108C (4) by replacing the *Bss*HIII-*Csp*45I segment with the same sequence including the insertion of ten histidine residues. *E. coli* F₁ with six histidine residues at the amino terminus of the α -subunit was prepared as described previously (5). Both the His₁₀- and His₆-engineered enzymes showed the same bulk properties as the non-engineered wild-type in ATP synthesis (*in vivo*) and ATP hydrolysis (*in vitro*).

Rotation assay

Immobilization of EF₁ onto a glass cover-slip and the attachment of observable markers to the γ -subunit (Fig. 1) were essentially as described previously (6). Markers ranged from single gold beads 40 to 200 nm in diameter (British BioCell, Cardiff, UK), to pairs of polystyrene beads each 220 to 495 nm in diameter (Polysciences, Warrington, USA). The 220 and 495 nm beads used were amine-modified and the 340 nm beads were carboxyl-modified. Polystyrene beads were biotinylated and bead-duplexes were prepared in the presence of 100 mM MgCl₂, followed by purification by gradient centrifugation, as described (6). His-tags were located at the *N*-termini of the α -subunits to ensure the preferred geometry for EF₁ surface immobilization. Ni²⁺NTA-coated cover-slips (6, 7) were used for extended observations of individual F₁ molecules labelled with bead-duplexes. For short observation times with small single gold beads, negatively-charged KOH-cleaned cover-slips were sufficient. An ATP-regenerating system, consisting of

1 mM phosphoenolpyruvate (Roche, Basel, Switzerland) and 50 $\mu\text{g/ml}$ pyruvate kinase (Roche), was used for all assays containing ATP. For assays with ATP γ S (Sigma-Aldrich, UK), a regenerating system was not used since its use would convert ATP γ S into ATP.

Rotation measurement

Depending on the size of the marker attached, different microscopy methods were employed. For 340 nm and 495 nm duplexes, a custom-built inverted bright-field microscope was used (6) and interlaced video images from a CCD camera (LCL-902K, Watec America Corp, Japan) were recorded at 25 Hz using a commercial DVD recorder (HD-A760-GX, Lite-On, Taiwan). For 220 nm duplexes, images were obtained using either bright-field microscopy and a high-speed CMOS camera (PCI-1024, Photron, San Diego, USA) at 200 Hz, or back focal plane laser-interferometry (6) sampled at 2 kHz. For single gold beads at low and high ATP concentrations, a commercial laser-based dark-field microscope was used as described (4) at frame rates up to 4 kHz and the bead position (x,y,t) was determined using MetaMorph (Molecular Devices Corp., Sunnyvale, CA). For gold beads at intermediate ATP concentrations, a custom laser-based dark-field microscope was used as described (9) at a frame rate of 22.5 kHz and the bead position (x,y,t) was determined using a MATLAB implementation of Gaussian Mask fitting (11).

External Torque

External torque was applied to 495 nm bead-duplexes attached to EF₁ by a custom-built optical tweezers set-up designed for the manipulation of rotary molecular motors (6) in the presence of 20 μM ATP.

Data conversion to polar coordinates

DVD files were converted to 25 Hz AVI files using the freeware package Auto Gordian Knot (<http://www.autogk.me.uk/>). The centroid of the image of a bead-pair (x,y,t) was calculated using custom-developed programs written in LabVIEW (National Instruments). Subsequent conversion into angle data,

$(x,y,t) \rightarrow (\theta,t)$, was achieved by fitting the (x,y,t) data to an ellipse (the projection of an arbitrary circular orbit onto the image plane).

Dwell Analysis

For molecules clearly displaying 120 degree step-like motion, a rudimentary analysis of step lengths was achieved using an algorithm that can be described as follows. Molecules rotating in step-like fashion displayed clear three-fold periodicity in the histograms of their dwell angles. Three equally-spaced boundaries were defined at or close to the minima in each histogram, taking into account slight deviations from perfect three-fold symmetry. Step lengths were then defined as the number of frames spent in each third of a revolution as the molecule rotated, multiplied by the temporal length of each frame.

For molecules at intermediate ATP concentrations, showing six dwell states per cycle, angle data was padded at each end then smoothed using an L1-PWC filter (10) with gamma set to 10 radians. A kernel density plot was then constructed from the dwell angle histogram, using a Gaussian kernel of sufficient width to give a smooth plot (4-7°). This was fit using the six-Gaussian peak function

$$n(\theta) = b + \sum_{i=1}^6 A_i e^{-\frac{(\theta-\theta_i)^2}{2w_i^2}}$$

The positions θ_i were used to define the location of each state and determine the angular separation between the catalytic and ATP binding dwell. The minima in the fit were used as boundaries to determine the edges of each state. Step lengths were then defined as the number of frames spent between each pair of dwell boundaries as the molecule rotated, multiplied by the temporal length of each frame

Calculation of the drag coefficient of beads attached to EF₁

We applied a geometrical argument to determine the drag coefficient of a single bead or a bead-duplex attached to a surface-immobilized EF₁ molecule. The average rotation rate is an important parameter, however this average rate includes molecule-to-molecule variation. We assumed that this variation is

mainly due to the different attachment angles of the probe. As a result, we calculated the average drag coefficient due to a population of probe attachment angles to compare against the average rotation rate.

A single biotinylated bead of radius r will attach to the streptavidin-EF₁ complex at a random angle. Consider Fig. 1a. Not all angular orientations (ϕ) will be possible due to the close proximity of the surface and the relatively large size of the bead compared to the streptavidin-EF₁ complex. If we assume that the surface is flat, the angular range of ϕ will range from ϕ_{\min} up to $\pi/2$, where $\sin(\phi_{\min}) = 1 - \frac{h}{r}$ and h is the height of the streptavidin-EF₁ complex. In our calculations we have taken $h=15\text{nm}$. The radius of rotation of a bead attached at an angle ϕ will be equal to $r\cos(\phi)$. Here, we will make the assumption that there are no preferred attachment angles, i.e., the angular distribution will be isotropic about a shell of solid angle $\Omega = 2\pi(1 - \sin(\phi_{\min}))$ and the density of states $n(\phi)$ will be proportional to $\cos(\phi)$. The mean gyration radius, $\langle R \rangle$, can then be calculated by

$$\begin{aligned}
 \langle R \rangle &= \frac{\int_{\phi_{\min}}^{\pi/2} R(\phi)n(\phi)d\phi}{\int_{\phi_{\min}}^{\pi/2} n(\phi)d\phi} \\
 &= \frac{\int_{\phi_{\min}}^{\pi/2} r\cos^2\phi d\phi}{\int_{\phi_{\min}}^{\pi/2} \cos\phi d\phi} \quad (\text{S1}) \\
 &= \frac{r^2}{2h} \left(\frac{\pi}{2} - \phi_{\min} - \frac{1}{2}\sin(2\phi_{\min}) \right)
 \end{aligned}$$

For a spherical bead of radius r rotating far from any surface about an axis d away from the bead center, the rotational drag coefficient is given by $\xi = 8\pi\eta r^3 + 6\pi\eta r d^2$, where η is the viscosity of water at room temperature ($10^{-9} \text{ pN nm}^{-2} \text{ s}$) (1). The average drag coefficient, $\langle \xi \rangle$, can then be found by

$$\begin{aligned}
\langle \zeta \rangle &= \frac{\int_{\phi_{\min}}^{\pi/2} \zeta_{r,t}(\phi) n(\phi) d\phi}{\int_{\phi_{\min}}^{\pi/2} n(\phi) d\phi} \\
&= \frac{\int_{\phi_{\min}}^{\pi/2} (8\pi\eta r^3 + 6\pi\eta r[r \cos \phi]^2) \cos \phi d\phi}{\int_{\phi_{\min}}^{\pi/2} \cos \phi d\phi} \quad (\text{S2}) \\
&= \frac{\pi\eta r^3}{h} (14[1 - \sin \phi_{\min}] - 2[1 - \sin^3 \phi_{\min}])
\end{aligned}$$

The average drag coefficients, calculated as per Equation S2, for the 40-200 nm single beads used in this study are shown in Supplementary Table S1.

When considering the geometry of a pair of beads attached to EF₁ we will simplify the calculations somewhat by assuming that the inner bead attaches at the average single bead gyration radius $\langle R \rangle$ as shown in Fig. 1b. The orientation of the bead-duplex itself will vary randomly and will, in general, form an angle θ with the surface with corresponding drag coefficient given by

$$\begin{aligned}
\zeta(\theta) &= (8\pi\eta r^3 + 6\pi\eta r \langle R \rangle^2) + (8\pi\eta r^3 + 6\pi\eta r (\langle R \rangle + 2r \cos(\theta))^2) \\
&= \pi\eta r [16r^2 + 12\langle R \rangle^2 + 24r^2 \cos^2 \theta + 24\langle R \rangle r \cos \theta] \quad (\text{S3})
\end{aligned}$$

Bead diameter used (nm)	Average drag coefficient of a single bead attached to EF ₁ (pN nm s)
40	0.00028
60	0.00087
80	0.0020
100	0.0037
200	0.028
Bead diameter used (nm)	Average drag coefficient of a bead-duplex attached to EF ₁ (pN nm s)
220	0.17
340	0.59
495	1.8

Supplementary Table S1: The average drag coefficient of the single beads and bead-duplexes used in this study calculated from Equation S2 estimated with no surface correction.

Assuming again that the bead-duplex has no preferential attachment angles, θ will be distributed isotropically about a hemispheric shell of solid angle 2π . If we assume that the drag coefficient of a bead-duplex is simply the linear combination of the drag coefficient for each of the two beads, then the average drag coefficient can be found in an analogous manner as for the single bead calculations to be

$$\begin{aligned}
\langle \zeta \rangle &= \frac{\int_0^{\pi/2} \zeta(\theta) n(\theta) d\theta}{\int_0^{\pi/2} n(\theta) d\theta} \\
&= \frac{\pi\eta r \int_0^{\pi/2} (16r^2 + 12\langle R \rangle^2 + 24r^2 \cos^2 \theta + 24\langle R \rangle r \cos \theta) \cos \theta d\theta}{\int_0^{\pi/2} \cos \theta d\theta} \\
&= \pi\eta r [32r^2 + 12\langle R \rangle^2 + 6\pi\langle R \rangle r]
\end{aligned}
\tag{S4}$$

The resulting drag coefficients for the 220 nm, 340 nm and 495 nm bead duplexes used in this study are presented in Supplementary Table S1.

Under conditions of high load and saturating [ATP] $v = \frac{T}{2\pi\zeta(\theta)}$. Using this relation and Equation S3

$$v = \frac{T}{2\pi} \frac{1}{16r^2 + 12\langle R \rangle^2 + 24r^2 \cos^2 \theta + 24\langle R \rangle r \cos \theta}
\tag{S5}$$

For simplification, we set $\langle R \rangle = 0$ to obtain

$$v = \frac{T}{2\pi} \frac{1}{16r^2 + 24r^2 \cos^2 \theta}
\tag{S6}$$

Under conditions of constant torque, Equation S6 reduces to Equation 5 in the main text,

$$v(\theta) = \frac{C}{2 + 3\cos^2 \theta}$$

Using the definition that the total number of molecules n_m is the same in both v - and θ -space, therefore

$$\int_{\theta} n(\theta) d\theta = \int_{v} n(v) dv, \quad \text{and the density of states in } v\text{-space can be expressed as } n(v) = n(\theta) \frac{d\theta}{dv}. \quad \text{Since}$$

$n(\theta) \propto \cos \theta$, an expression for the density of states in v -space can be the density of states in θ -space

given by

$$N(v) = \frac{n_m P}{2\sqrt{3}v^2} \left(5 - \frac{P}{v}\right)^{-1/2} \quad \text{for } \frac{P}{5} \leq v \leq \frac{P}{2} \quad (\text{and } N(v) = 0 \text{ otherwise}). \quad (\text{S7})$$

S7 is also given as Equation 6 in the main text. P in Equation S7 is the equivalent speed of a single bead attached to EF1 rotating about its own axis. Due to the range of angles available to the duplex, the maximum speed is observed when the beads are stacked on top of each other ($\theta = \pi/2$). Since the geometry of such a duplex is known, an estimate of the torque can be obtained from $T = 16\pi^2 \eta r^3 P$.

In the main text, we show histograms of the observed rotation rates for different marker sizes (Fig. 3b). Equation S7 is a continuous function. We made Equation S7 discrete by integrating over the width of the histogram bins.

$$H(v) = \frac{n_m}{\sqrt{3}} \left[\left(5 - \frac{P}{v}\right)^{1/2} \right]_a^b \quad \text{for } \frac{P}{5} \leq v \leq \frac{P}{2} \quad (\text{and } H(v) = 0 \text{ otherwise}), \quad (\text{S8})$$

Where b and a are the upper and lower edges of each histogram bin. We fitted Eq. S8 to the histograms in Fig. 3b. Errors on the fitting parameter P were obtained by the method of bootstrapping with 1000 random resamples of the dataset with replacement.

Drag coefficients obtained in the manner described above will be an underestimate of the true drag due to the close proximity of the coverslip surface (1). The exact correction for a bead or bead-duplex attached to F_1 has not been attempted. Instead, we corrected for single beads of radius r a distance h away from a non-slip surface. We have defined the drag correction factor (CF) to be $CF = \frac{\zeta_s}{\zeta_o}$, where ζ_o and ζ_s are the drag coefficients far from a surface and close to a surface respectively. For a bead moving parallel to the surface, CF is given by (1, 2)

$$CF_T = \frac{1}{1 - \frac{9}{16}\left(\frac{r}{h}\right) + \frac{1}{8}\left(\frac{r}{h}\right)^3 - \frac{45}{256}\left(\frac{r}{h}\right)^4 + \dots} \quad (\text{S9})$$

and for a bead rotating about an axis perpendicular to the surface (1)

$$CF_R = \frac{1}{1 - \frac{1}{8}\left(\frac{r}{h}\right)^3 + \dots} \quad (\text{S10})$$

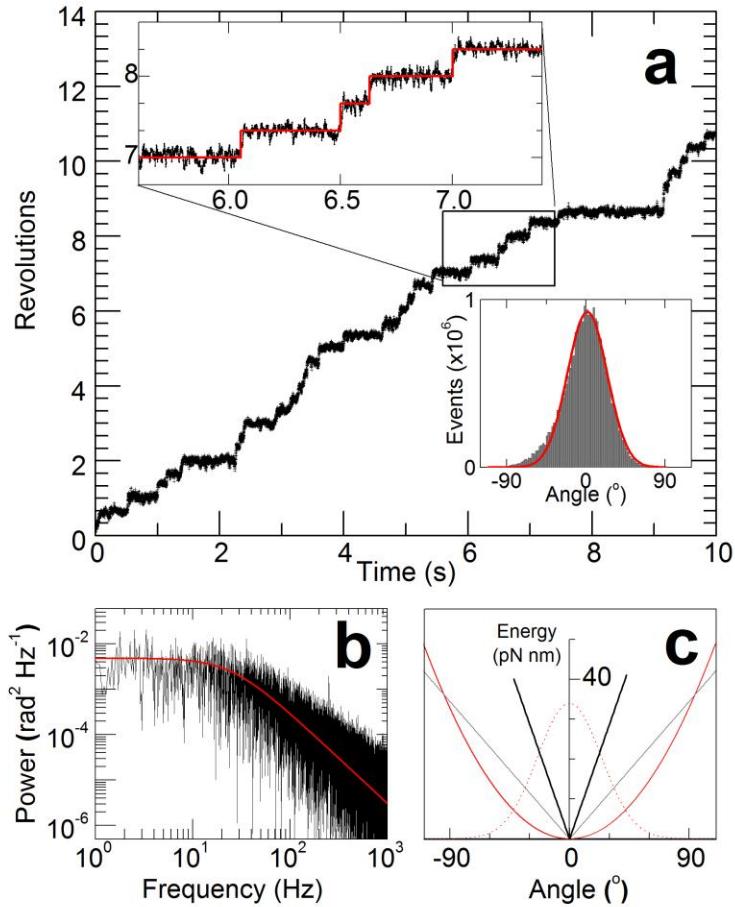
CF_T for pure translation (Equation S9) is significantly higher than CF_R for pure rotation (Eq. S10). Assuming that the drag due to a bead-duplex is the sum of the drag of each of the two beads, the surface correction required for a bead-duplex is substantially more than for a small (40-100 nm) single bead due to the large radius of gyration of the outer bead in the duplex. Taking into account Equations S9 and S10 and the geometrical discussions above, the drag with surface corrections can be expressed as

$$\xi(\theta, h, r) = CF_R^{inner} 8\pi\eta r^3 + CF_T^{inner} 6\pi\eta r \langle R \rangle^2 + CF_R^{outer} 8\pi\eta r^3 + CF_T^{outer} 6\pi\eta r (\langle R \rangle + 2r \cos \theta)^2 \quad (\text{S11})$$

where CF^{inner} and CF^{outer} are the correction factors from Eqs. S9 and S10 calculated for the inner and outer beads as a function of the bead's distance from the surface. Consideration of Fig. 1 shows that CF^{inner} is only a function of r and h whereas CF^{outer} is a function of r , h and θ . An equation similar to Eq. S4 results

in an estimation of the surface-corrected drag coefficient. Using numerical integration we calculate that the proximity of the surface will increase the mean drag coefficient of the bead-duplexes by 40% ($CF = 1.4$) for the bead-duplexes used in this study. Considerably larger drag coefficients are possible, however, if the bead duplexes interact directly with the surface, as has been shown for actin filaments (3). Unless otherwise stated, we used the drag coefficients calculated in the absence of a surface (see Table S1) but then took care to note the requirement for the surface correction factor.

Estimation of the angular stiffness of the ATP-binding state in EF₁



Supplementary Figure S1: An estimate of the angular stiffness of the ATP-binding state. (a) At 120 nM ATP and with a 220 nm bead-duplex, EF₁ undergoes clear stepping rotation as shown in the upper inset (red line is the result of step fitting). The angular distribution whilst in the dwell state (see lower inset) is Gaussian in shape ($N(\theta) = A \exp(-(\theta - \theta_0)^2 / 2\sigma^2)$ with $\sigma = 22.5 \pm 1.1^\circ$, $A = 963 \pm 12$ and $\theta_0 = 1.6 \pm 0.3^\circ$) suggesting that the profile experienced by the bead-duplex is parabolic. Note that our detection noise has a standard deviation of less than 0.5° (data not shown). The effective spring constant K_f describing the width of the state ($U = \frac{1}{2}K_f\theta^2$) can be calculated from the Boltzmann distribution ($P \propto e^{-U/k_B T}$) to be $K_f = 26.5 \pm 1.8$ pN nm rad². (b) The one-sided power spectrum of the angular fluctuation during the dwells (black line). The spectrum is Lorentzian in shape, $S(f) = \frac{S_0}{1 + f^2/f_c^2}$, with

characteristic corner frequency $f_c = K_f / 2\pi\zeta$. Obtained parameters from a non-linear curve fit (thick red line) are $S_0 = (5.5 \pm 0.2) \times 10^{-3} \text{ rad}^2 \text{ Hz}^{-1}$ and $f_c = 25.2 \pm 1.1 \text{ Hz}$. (c) The potential energy curve for the 220 nm bead-duplex in the ATP-waiting state (red curve) as compared to the potential energy curves expected from a constant motor torque profile of 21.9 pN nm (grey line) or 50 pN nm (black line). Overlaid is the Gaussian distribution (dotted red curve) found in (a) to demonstrate the range of the experimental angular freedom.

We estimated the angular stiffness of the ATP-binding state from the angular Brownian motion of the robe during dwells. Supplementary Fig. S1a shows step-wise rotation of EF₁ at 120 nM ATP, sampled at 2 kHz using back-focal-plane interferometry (see Methods in the main text) and a 220 nm bead-duplex. We applied a 50-point running mean filter and assigned each filtered data point to the closest of three equally-spaced dwell angles (red line, upper inset). We calculated the histogram (Fig. S1a, lower inset) and power spectrum (Fig. S1b) of Brownian motion during dwells, defined as the difference between the probe angle and the assigned dwell angle. The power spectrum confirms that the distribution is well sampled, and a Gaussian fit to the histogram (red, $\sigma = 22.5 \pm 1.1^\circ$) gives $K_f = 26.5 \pm 1.8 \text{ pN nm rad}^{-2}$ for the linear stiffness of the dwell state, by the principle of equipartition of energy. Fig. S1c shows the dwell state potential (red), the Brownian angle distribution (dotted red) and linear potentials corresponding to constant torque of 21.9 pN nm (our lower bound estimate, grey) or 50 pN nm (our upper bound estimate (3), black). The dwell-state spring would need to be extended by an angle $\phi = T/K_f = 47^\circ$ or 108° to exert a torque of 21.9 or 50 pN nm respectively. Note, however, that part of our measured compliance may be in the linkers between the surface or probe and EF₁, as well as within EF₁ itself.

The data of Supplementary Fig. S1 allow direct calculation the drag coefficient of this particular bead duplex as $\zeta = K_f / 2\pi f_c = 0.17 \pm 0.02 \text{ pN nm s}$, similar to the average drag coefficient predicted for this size of bead duplex neglecting surface interactions ($\zeta = 0.17 \text{ pN nm s}$, see above). Thus this particular duplex either had negligible surface interaction or a larger than average azimuthal angle (θ in Fig. 1b in the main text) leading to a lower than average drag coefficient.

Fitting of dwell time distributions

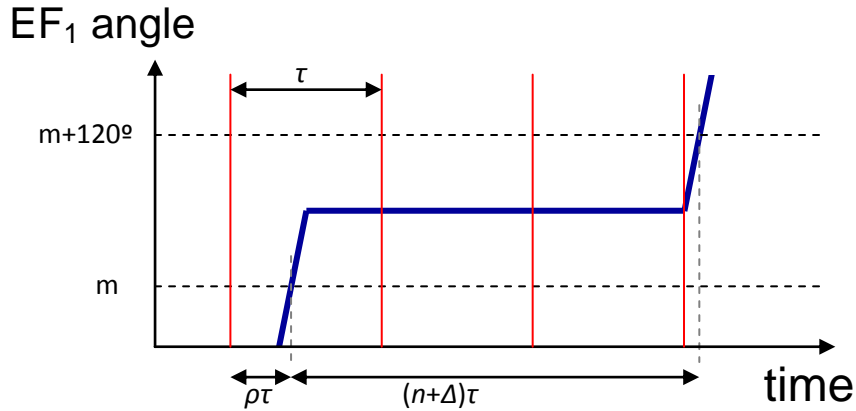
(1) 120° steps at low [ATP]

We obtained the apparent unimolecular rate constant of ATP binding (k_{ATP}) from the set of step dwell times by a maximum likelihood estimation approach, i.e., by minimization of the negative log-likelihood function $L(k_{\text{ATP}}) = -\sum_i \ln p(t_i)$, where t_i is the set of dwell times generated by the exponential probability function $p(t_i) = k_{\text{ATP}} \exp(-k_{\text{ATP}} t_i)$.

(2) 120° steps at high [ATP]

The dwell time of the catalytic state of EF₁ is comparable to the temporal resolution of our experimental set-up. More accurately, the average catalytic dwell was approximately three times longer than the frame time (and exposure time) of the camera used [in frame transfer mode] in this study. As a result, effects due to the averaging nature of the image have been taken into account, as outlined in the following discussion.

To determine the time spent by rotating EF₁ (single 40-60 nm beads) within each 120° arc, the angular position of EF₁ was determined for each camera frame, and classified as lying within one of three 120° arcs centered on the position of the catalytic dwell. Dwell times were calculated by summing the number of frames observed in each arc during one period of rotation, and multiplying by the temporal length of a frame (0.25 ms for data at 4 kHz). While we observe a dwell lasting for a discrete number of frames, the underlying distribution of enzyme dwells must be continuous. It is thus important to consider the manner in which the dwell times are discretely sampled to correctly fit a kinetic model to the observed dwell distribution.



Supplementary Figure S2: Diagram of the angular position of EF_1 passing through a dwell of length $(n+\Delta)\tau$, for $n = 2$ and $\Delta \sim 0.7$. Camera frames last a period τ , with red lines marking the beginning of each new frame. The offset between the beginning of a camera frame and the beginning of a dwell is $\rho\tau$, with $\rho \sim 0.4$ in this figure and $0 < \rho < 1$ in general. The number of frames which the enzyme is observed to spend at a dwell angle will be either n or $n+1$, depending on the values of ρ and Δ .

If we consider a dwell which actually lasts $n + \Delta$ frames each of length τ (n integral, $0 \leq \Delta < 1$), upon sampling it may be observed to last either n or $n+1$ frames. The probability of each of these observations can be calculated by considering the temporal offset between the triggering of the camera frame and the beginning of the enzyme dwell, ρ (in fractions of τ , such that $0 \leq \rho < 1$) as marked as in Supplementary Fig. S2. An inspection of Supplementary Fig. S2 will show that, for the case $\Delta \leq 0.5$, then if $(0.5-\Delta) < \rho < 0.5$, the enzyme will appear to be observed at the dwell for $n+1$ frames, while for other values of ρ the enzyme will be observed at the dwell for n frames. For the case of $\Delta > 0.5$, $n+1$ frames will be observed for either $0 \leq \rho < 0.5$ or $\rho > (1.5-\Delta)$, and n frames otherwise. We assume that, over many dwells, the offset ρ will be uniformly distributed over $[0,1)$, and hence that the probability of observing n frames for a dwell of actual length $n + \Delta$ frames, is proportional to the fraction of possible values of ρ which lead to this observation. This gives a probability of $(1-\Delta)$ to observe n frames, and the probability of Δ to observe $n+1$

frames. This allows us to calculate the fractional number of observations of dwells lasting n frames, for a given kinetic model where the probability of a dwell lasting a time t is $p(t)$, as:

$$P(n) = \int_{(n-1)\tau}^{(n+1)\tau} p(t) \left(1 - \frac{|t - n\tau|}{\tau} \right) dt, \quad n \geq 0 \quad (\text{S12})$$

We evaluated Equation S12 using the two parameter model described in the main text, $p(t) \propto [\exp(-k_1 t) - \exp(-k_2 t)]$, with the integral evaluated analytically to determine the expected distribution of dwell times for given values of k_1 and k_2 . A two parameter optimization procedure was carried out to determine the values of k_1 and k_2 which best fit the observed dwell probability distribution, using the MATLAB function *fminsearch* to minimize the sum of squared errors of the observed and expected dwell distributions, with the result plotted as the red dotted line in Fig. 5c. The same procedure was also carried out to fit a second model, $p(t) \propto [\exp(-k_1(t - \tau_m)) - \exp(-k_2(t - \tau_m))]$ for $t > \tau_m$ ($p(t)=0$ otherwise), using a three parameter (k_1, k_2, τ_m) optimization, and the result is shown as the blue line in Fig. 5c. Uncertainties in the fitting parameters were calculated from the associated covariance matrix.

Dwell data for EF₁ in the presence of ATP γ S is shown in Fig. 5d. The histogram bins were set to a width of two frames (each 1 ms) in order that each bin contained a significant number of dwells. Because each bin corresponds to a range of possible number of frames observed, the approach used above becomes invalid. Instead, we make the simplifying assumption that when the histogram bin size is larger than τ , the allocation of dwell times to bins becomes perfect. That is:

$$P(n) \cong \int_{t_{\text{lower}}(n)}^{t_{\text{upper}}(n)} p(t) dt \quad (\text{S13})$$

where $t_{\text{lower}}(n)$ and $t_{\text{upper}}(n)$ are the lower and upper bounds of bin n . The distribution of dwells for EF₁ in the presence of ATP γ S was fit as above, with Equation S10 replaced by Equation S13, for a two

parameter kinetic model. The optimal fit is shown in Fig. 5d. The rate constants and their uncertainties are quoted in the main text.

(3) 35° steps at intermediate [ATP]

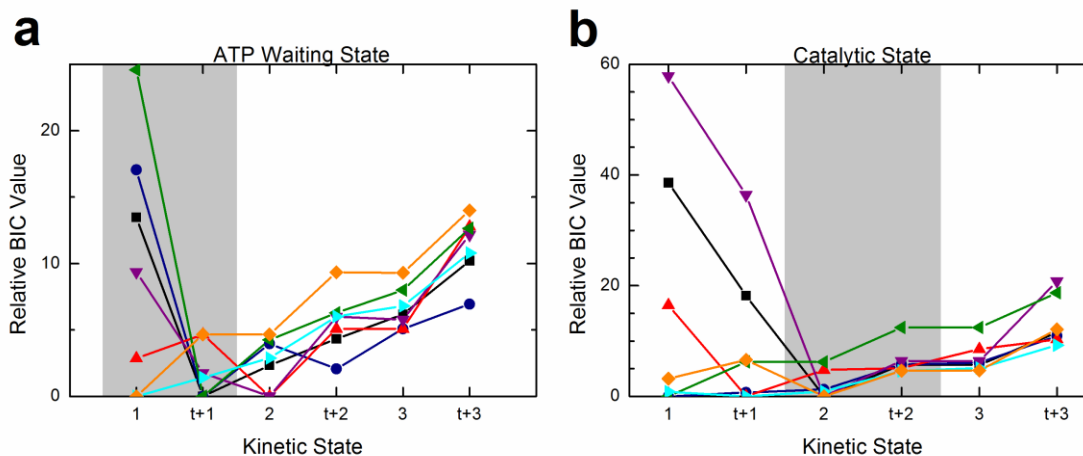
Interpreting the data collected at intermediate [ATP] is complicated by the overlap of data from neighbouring dwell states. This makes it difficult to determine dwell times without contaminating the dwells measured for one state with information from neighbouring states.

To attempt to minimise this contamination, we smoothed the data using a steppy filter (L1-PWC, padded at ends, $\gamma = 10$ radians, (10)) prior to binning into dwells. Any dwell lasting longer than 15 ms was attributed to a pause and removed (dwells typically lasted 0-2 ms). We then determined maximum likelihood (MLE) fits to the resulting dwell histograms using the equation (S12). The likelihood of six fitting models – comprising one, two or three kinetic parameters with and without an additional time offset parameter – were compared using the Bayesian Information Criterion (12):

$$BIC = -2\log_e L + k \log_e n$$

(S14)

Where $-\log_e L$ is the negative log likelihood from the MLE fit, k is the number of fitting parameters and n is the number of data points fit (number of observed dwells, ranging between 99 and 585).



Supplementary Figure S6: Comparison of kinetic models fit to data at intermediate [ATP] showing six visible dwell angles. Fits to ATP waiting dwells are shown in (a), fits to catalytic dwells in (b). The relative BIC value (a measure of the quality of the model, lower is better, see Equation S14) is plotted versus the different kinetic models for each bead, with each bead shown in a different colour. For each state, between 1 and 3 kinetic parameters were fit with or without a time-offset parameter that would correspond to the time spent rotating a bead between dwells (this rotation period is not removed from the dwell times). There is no unique model which is the best fit to all data traces, however clear trends in model fits are visible. (a) The ATP waiting state is typically well fit using either one kinetic parameter and a time offset, or by two kinetic parameters. The Catalytic dwell state (b) is typically best fit with two kinetic parameters. The regions shaded grey in each figure correspond to the models which best match those observed at (a) low [ATP] and (b) high [ATP].

The results are presented in Supplementary Fig S6. Although the best-fitting state is not consistent between beads, the catalytic state was typically well fit with two kinetic parameters (best model in 5/7 cases), and the ATP binding state was typically fit well with two kinetic parameters (best model in 2/7 cases), or one kinetic parameter and a constant transition time offset (best model in 3/7 cases). In the instances where the two kinetic parameter fit was the preferred model, one of the parameters was very fast (8.6 ms^{-1} and 28 ms^{-1}) and hence not dissimilar to a sub-millisecond time offset. We therefore conclude that the observations are consistent with a two kinetic parameter model for the catalytic state and a one kinetic parameter model for the ATP binding state, but that we do not have sufficient resolution to extract the dwells accurately at intermediate ATP concentrations.

Finally, we note that, to the best of our knowledge dwell analysis has not previously been performed on any F_1 at intermediate ATP concentrations. The task of extracting these dwells is more difficult for EF_1 than TF_1 for two reasons. Firstly, EF_1 has a lower observed stiffness, and hence there is greater overlap in the observed bead position between states. Secondly, there is less scope for averaging or filtering to improve the accuracy of dwell angle recovery in EF_1 because the dwells last, on average, one-quarter as long, and the relaxation time of the bead (inversely proportional to stiffness) is longer.

Simulation of high speed data

As an additional verification of the fitting process described in the previous section, a computer simulation was constructed to generate data similar to that collected at high [ATP] with single 60 nm beads. This simulation is described in two parts: (a) the generation of information about the angular state of EF_1 , and (b) the conversion of this information to (x,y,t) coordinates suitable for analysis in the same manner as experimental data.

The angular position of EF_1 was modeled as consisting of five rate processes per 120° rotation (or equivalently, fifteen processes with three fold symmetry per revolution). These processes consisted of:

1. A dwell at angle 0° (or equivalently, 120 or 240°), of duration randomly selected from an exponential distribution of rate $8.6 \times 10^4 \text{ s}^{-1}$, the estimated rate for ATP binding at 2 mM concentration.
2. Smooth rotation of angle between 0° and 80° , over a time period of $55\mu\text{s}$, which is equivalent to the rotation rate expected for a 60nm bead rotated with a constant torque of 21.9 pN nm.
3. A dwell at angle 80° of duration randomly selected from an exponential distribution of rate (a) $2.5 \times 10^3 \text{ s}^{-1}$, the estimated rate for ATP hydrolysis or (b) 88 s^{-1} , the estimated rate for $ATP\gamma S$ hydrolysis.
4. A dwell at angle 80° , of duration randomly selected from an exponential distribution of rate (a) $3.3 \times 10^3 \text{ s}^{-1}$ or (b) 320 s^{-1} , the estimated rates for phosphate release with ATP and $ATP\gamma S$ respectively.
5. Smooth rotation of angle between 80° and 120° , over a time period of $28\mu\text{s}$, which is equivalent to the rotation rate expected for a 60 nm bead rotated with a constant torque of 21.9 pN nm.

Note that the assignment of the two rates in steps 3 and 4 can be reversed with no effect on the model as there is no change in the F_1 position between states 3 and 4. Additionally, the rate constant for ATP

binding is sufficiently fast that the dwell at 0° (process 1) is negligible compared with the other processes, and the transition is essentially a 120° transition of constant angular speed. The ATP binding step is, however, included explicitly for completeness.

After completion of each set of five rate processes, the enzyme is considered to reset and cycle through the same processes at angles 120° beyond those of the previous cycle.

The angular information generated about EF_1 was then converted into (x,y,t) data. This conversion accounted for both the effect of Brownian motion on the EF_1 -bead system, and the imaging system, as follows:

The bead was modelled as being connected to the enzyme via a torsional spring of constant κ_θ , such that the torque T on the bead is given by $T = \kappa_\theta(\theta_{F1} - \theta_{bead})$. Additionally, the bead was considered subject to a Wiener process (Brownian motion), inducing a movement of the bead with amplitude:

$$\Delta\theta = Z\sqrt{2Ddt} \quad (S14)$$

in the limit $dt \rightarrow 0$, where dt is the time period, D is the diffusion coefficient of the bead ($= k_B T / \xi$ for Boltzmann constant k_B and temperature T) and Z is a normally distributed random variable of mean zero and unit variance. Computationally, this was implemented as:

$$\theta_{bead}(t + \Delta t) = \theta_{bead}(t) + \frac{\kappa_\theta(\theta_{F1} - \theta_{bead})}{\xi_{bead}} \Delta t + Z \frac{1}{\kappa_\theta} \left(1 - e^{-\frac{2\kappa_\theta \cdot k_B T}{\xi_{bead}} \Delta t} \right) \quad (S15)$$

where the last term in Equation S15 is equivalent to Equation S14 for $\Delta t \rightarrow 0$, but includes an appropriate damping term for larger Δt values.

The observed position of the gold bead varies both in angle and radius. It was assumed that these variations are independent, and that radial variation is also governed by a Wiener process driving the bead on a damped spring, such that the radial position of the bead is given by:

$$r_{bead}(t + \Delta t) = r_{bead}(t) + \frac{\kappa_r (r_0 - r_{bead})}{\xi_{bead}} \Delta t + Z \frac{1}{\kappa_r} \left(1 - e^{-2 \frac{\kappa_r \cdot k_B T}{\xi_{bead}} \Delta t} \right) \quad (\text{S16})$$

for some r_0 , which is approximately the mean radius of the bead's motion. The initial values of θ_{bead} and r_{bead} were set to $\theta_{bead}(t=0) = 0^\circ$ and $r_0 = 20$ nm respectively.

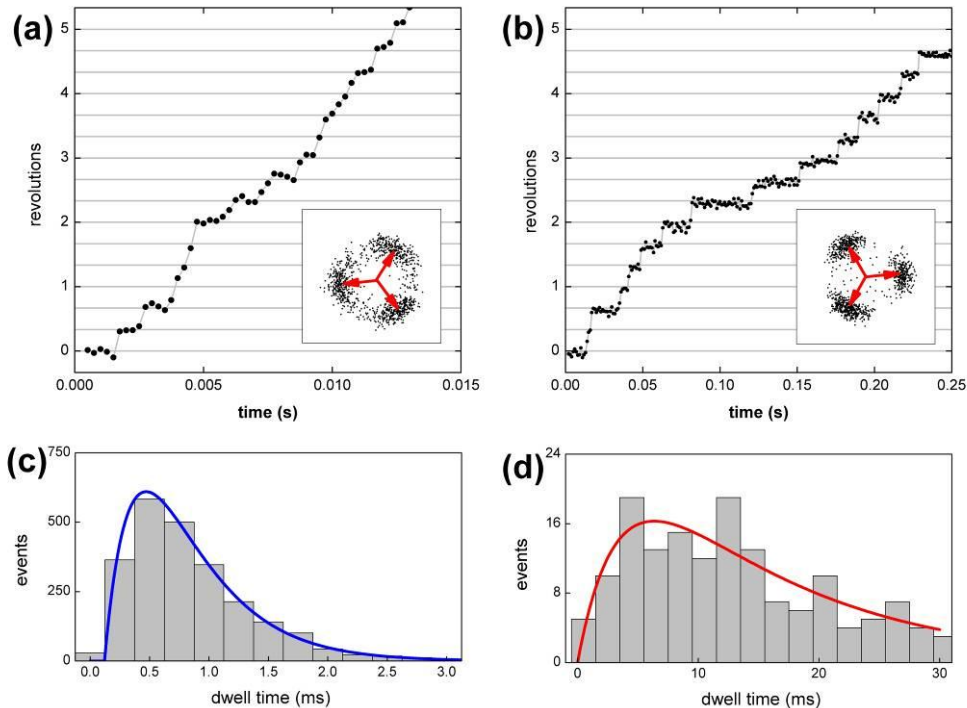
The location of the bead, as viewed in the microscope, was assumed to be given at any time by:

$$\begin{aligned} x &= r_{bead} \cos(\theta_{bead} + \varphi) \\ y &= r_{bead} \sin(\theta_{bead} + \varphi) \end{aligned} \quad (\text{S17})$$

where φ is a fixed offset angle, randomly selected in the range $0^\circ < \varphi < 360^\circ$.

Although analytic forms for the mean angular position of the bead, subject to the above processes during a known time window, can be derived, we are not aware of such an expression for the mean x and y

coordinates during a time window subject to the above equations. Therefore, we use Equations S15, S16 and S17 with $\Delta t = 1 \times 10^{-7}$ s to evaluate the location of the attached bead every timestep of length Δt , using the angular positions for EF_1 derived earlier. The position recorded in each camera image frame was assumed to be the mean value of x and y recorded at every timestep during the camera frame. Camera frames were assumed to last 0.25 ms ($2500 \times \Delta t$) for ATP data (4 kHz) and 1 ms ($10^4 \times \Delta t$) for $ATP\gamma S$ data (1 kHz), and to have no time delay between frames. This model was coded in C++ and evaluated to generate x and y data of similar length to that used for fitting dwell distributions to experimental data (8000 frames for ATP, 3000 frames for $ATP\gamma S$). Computational run time was < 10 s.



Supplementary Figure S3: An example of the simulated (x,y,t) data generated for (a) 2 mM ATP and (b) 1 mM $ATP\gamma S$ with a single 60 nm bead attached. The main graphs show the angular position over time and the insets show the xy orbits with the dwell positions indicated by red arrows. The distribution of dwell times fit for these traces, using the same methods as for the experimental data, are shown in (c) and (d) respectively. (c) The distribution of dwell times for EF_1 with 2 mM ATP are well fit by a three parameter kinetic model, with, for the data shown, $\tau_m = 0.121 \pm 0.005$ ms, $1/k_1 = 0.44 \pm 0.03$ ms and $1/k_2 = 0.28 \pm 0.03$ ms. (d) The simulation of $ATP\gamma S$ involves longer dwell times, making the transition time unresolvable. Supplementary Table S2 summarises the results of fitting ten such simulations for both ATP and $ATP\gamma S$.

The values for κ_θ and κ_r are not known from experiment, although it was estimated that κ_θ for 60nm gold beads would be of the same order of magnitude as the value given in the main text for large beads (26.5 pN nm rad⁻²). Using this value as an initial estimate, values were selected such that the xy plots of simulated data (Supplementary Fig. S3a-b) were similar, by eye, to those from experiment. We used values of $\kappa_\theta = 9.4$ pN nm rad⁻² and $\kappa_r = 1.4$ pN nm⁻¹.

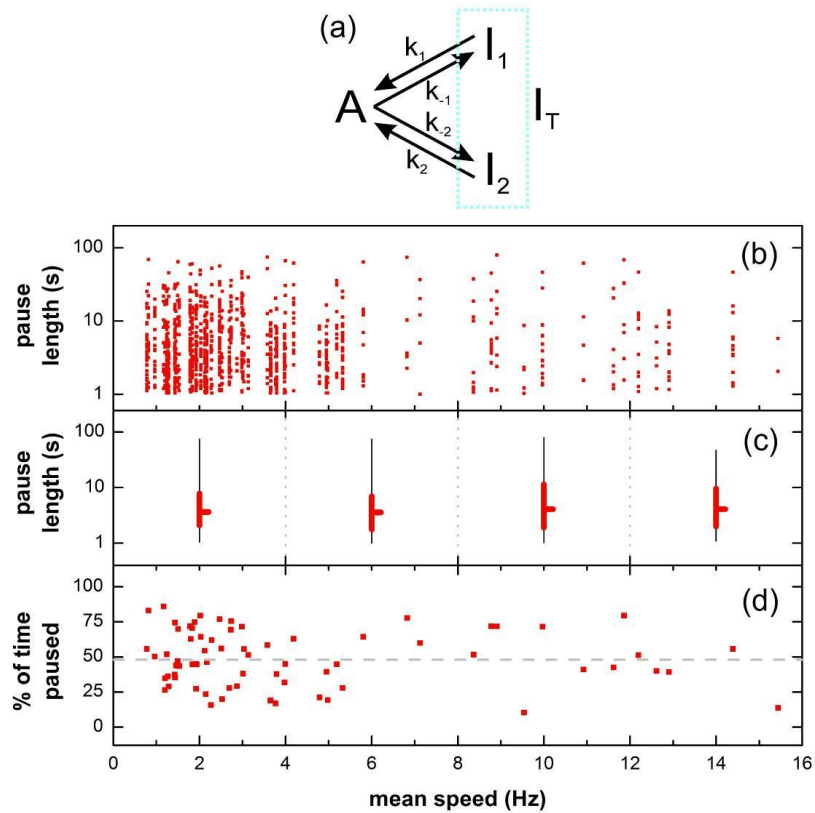
Kinetic Parameter	Experiment recovered value	Simulation value	Mean \pm sample deviation of recovered value (n=10)
ATP 2s ~ 2500 dwells			
τ_m	0.13 \pm 0.01 ms	0.083 ms	0.120 \pm 0.012 ms
1/ k_1	0.41 \pm 0.07 ms	0.40 ms	0.42 \pm 0.06 ms
1/ k_2	0.29 \pm 0.07 ms	0.30 ms	0.32 \pm 0.06 ms
ATPγS 3s ~ 210 dwells			
1/ k_1	11.3 \pm 1.7 ms	11.3 ms	10.2 \pm 2.3 ms
1/ k_2	3.1 \pm 0.7 ms	3.1 ms	3.8 \pm 1.5 ms

Supplementary Table S2: Kinetic parameters recovered from analysis of 10 EF₁ simulations in the presence of either ATP or ATP γ S (column 4), and the equivalent parameter used within the simulation (column 3). One such simulation is shown in Supplementary Fig. S3. The parameters recovered from analysis of the simulated experimental data are shown in column 2.

The (x,y,t) data from this simulation was analyzed in the same manner as the experimental data to produce dwell time histograms and kinetic fit parameters as shown in Supplementary Fig. S3c-d. Fit parameters were calculated for ten simulations each of ATP and ATP γ S data, and were shown to recover the kinetic parameters (k_1 and k_2) within the model with high accuracy (**Supplementary** Table S2). The variation in recovered parameters is similar to the errors quoted for the fit to experimental data. The temporal offset for high ATP simulation data consistently overestimated the transition time by approximately 50%, suggesting that the transition time fit to experimental data of 0.13 ± 0.01 ms may be an overestimate. This remained true for simulations with shorter (0.045 ms) transition times, whereby the fitted time was reduced, but remained $\sim 50\%$ higher than the simulated transition time). The cause of this offset is not known, but may relate to imperfect recovery of very short dwells.

In summary, the simulations showed that the method used to recover kinetic parameters from histograms of dwell distributions give unbiased estimates for the kinetic parameters k_1 and k_2 , with variation in fit values similar to estimated errors, but may overestimate the transition time τ_m by up to 50%.

Calculation of the rates to and from the inhibited state



Supplementary Figure S4: The inhibited state of EF₁. (a) The inhibited state I_T appears to be two unresolved states I₁ and I₂ which decay back into the active state A with rates k_1 and k_2 respectively. At equilibrium, the active state A will convert into one of the inhibited states with rates k_{-1} and k_{-2} and the fraction of molecules in each state will be unchanging. The EF₁ inhibited state showed no dependency on the size of the viscous load attached. (b) The lengths of the pauses observed as a function of the mean rotation speed (excluding periods of pauses). (c) A box plot showing the full range of the pauses observed (grey line), the interquartile range (red line) and the median value (red central tick) for molecules in classes 0-4 Hz, 4-8 Hz, 8-12 Hz and 12-16 Hz. (d) The fraction of time paused *versus* the mean rotation rate showed negligible correlation (correlation coefficient -0.03) with a mean value of 48.6%. Correcting for unobserved pauses shorter than 1 s, EF₁ spent ~50% of its time paused at 2 mM ATP.

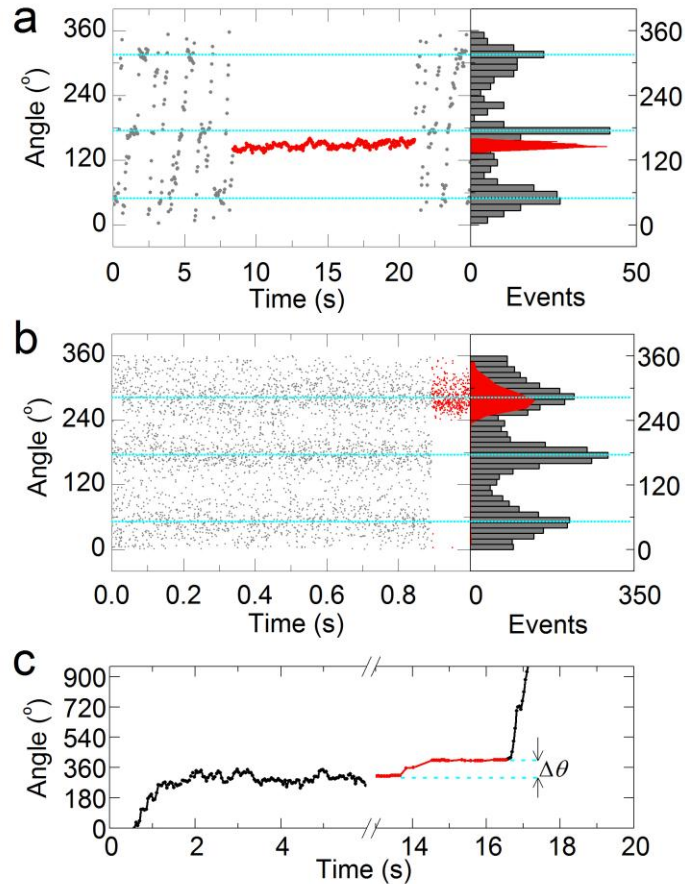
The dynamic equilibrium proposed in the main text between two unresolved inhibited states and the active state is summarized in Supplementary Fig. S4a. If F_A , F_1 and F_2 are the fraction of molecules in the active state, inhibited state 1 and inhibited state 2 respectively with $F_a + F_1 + F_2 = 1$, the relative populations of paused and rotating molecules will be unchanging at equilibrium. Therefore

$$\begin{aligned}
F_a k_{-1} &= k_1 F_1 \\
F_a k_{-2} &= k_2 F_2
\end{aligned}
\tag{S18}$$

F_a , F_1 and F_2 can be calculated from Equation 12 in the main text and from the total fraction of time EF₁ spends paused (f_p). Solving for k_{-1} and k_{-2} gives

$$\begin{aligned}
k_{-1} &= \frac{p_1}{p_1 \tau_1 + p_2 \tau_2} \frac{f_p}{1 - f_p} \\
k_{-2} &= \frac{p_2}{p_1 \tau_1 + p_2 \tau_2} \frac{f_p}{1 - f_p}
\end{aligned}
\tag{S19}$$

Analysis of the angle of the paused state of EF1



Supplementary Figure S5: The paused state of EF₁ is at determined angles relative to the active dwell states and can be re-activated by the application of external torque. (a-b) The position of the long pauses (see Methods for definition of a ‘long pause’) relative to the ATP-binding dwell state (a) and catalytic dwell state (b). For 11 pauses relative to the ATP-binding state, the mean pause angle was $82 \pm 3^\circ$ in the forwards direction from the ATP-binding dwell. For 7 pauses relative to the catalytic dwell, the pause angle was $2 \pm 4^\circ$ forward from the catalytic dwells. (c) Re-activation of EF₁ out of the paused state by manipulation with an optical trap. The trap was used to rotate the molecule 100° in the forwards direction relative to the pausing angle (indicated by $\Delta\theta$). The time during which the trap was applied is shown in red. When the trap was switched off at $t=16.6$ s, the EF₁ molecule was in the active state.

76% of the molecules (55 out of 72) studied showed preferential angles for pausing, with over two-thirds of these molecules displaying clear pauses at angles separated by $\sim 120^\circ$. The remaining molecules

presumably had a loose linkage either between the γ -subunit and the probe or between the surface and the EF₁ molecule. Pauses were nonetheless constrained within 1 revolution and the paused state was easily distinguished from the rotating state. To investigate the angle of the pauses relative to known states within the EF₁ catalytic cycle, records exhibiting 120° step-wise rotation (either due to ATP-binding or catalytic dwells) were analysed for pauses that were too long to belong to the underlying stepping distribution. To differentiate between pauses and the ATP-binding/catalytic dwells the following criteria were imposed. In the case of ATP-binding assays ($[ATP] < K_M$), the probability of observing an ATP-binding dwell of length t is known and given by $p(t) = k_{ATP} \exp(-k_{ATP}t)$, where k_{ATP} can be determined from $k_{ATP} = k_{on}[ATP]$ and the experimentally derived k_{on} . In the case of the catalytic dwell assays (saturating ATP), the probability of observing a catalytic dwell of length t is given by $p(t) \propto [\exp(-k_1t) - \exp(-k_2t)]$, using our experimentally derived parameters (k_1 , k_2 , and T_m). Long dwells were defined as pauses if the probability of the dwell belonging to the ATP-binding or catalytic dwell distributions was very low ($\int_t^\infty p(t)dt < 10^{-4}$).

11 pauses relative to the ATP-binding state and 7 relative to the catalytic dwell state were found. Two examples are shown in Supplementary Fig. S5a-b. The average pause angle was $82 \pm 3^\circ$ forwards of the ATP-binding state, and $2 \pm 4^\circ$ forwards of the catalytic state. Using the paused state as a reference marker suggests that the EF₁ catalytic state is at a position of $80 \pm 5^\circ$ forwards from the EF₁ ATP-binding state. Because we analysed only pauses that were statistically determined to be long, there remains a possibility that only the longer pause state has been analysed. Thus this state at least can be attributed to failure of product release at the catalytic dwell angle. If none of the pauses identified in stepping records were of the shorter type, the possibility remains that the short pause is due to ADP binding at the ATP-waiting angle.

We used an optical trap to apply external torque to paused EF₁ molecules. Torque was applied to 495 nm bead-duplexes attached to EF₁ by a custom-built optical tweezers set-up designed for the manipulation of

rotary molecular motors (6) in the presence of 20 μM ATP. 8 of the 15 molecules studied were successfully re-activated by forced forwards rotation during a pause. One example is shown in Fig. S5c. This external manipulation is thought to unzip the binding site to the inhibitory Mg^{2+}ADP (8). From our results, it appears that the probability of re-activation is dependent upon the degree of forwards rotation in agreement with an angle-dependent affinity of the Mg^{2+}ADP molecule to the binding pocket.

References

1. Happel, J. a. B., H. 1963. *Low Reynolds Number Hydrodynamics*. Martinus Nijhoff Publishers, The Hague.
2. Svoboda, K., and S. M. Block. 1994. Biological applications of optical forces. *Annu Rev Biophys Biomol Struct* 23:247-285.
3. Panke, O., D. A. Cherepanov, K. Gumbiowski, S. Engelbrecht, and W. Junge. 2001. Viscoelastic dynamics of actin filaments coupled to rotary F-ATPase: angular torque profile of the enzyme. *Biophys J* 81:1220-1233.
4. Nakanishi-Matsui, M., S. Kashiwagi, H. Hosokawa, D. J. Cipriano, S. D. Dunn, Y. Wada, and M. Futai. 2006. Stochastic high-speed rotation of *Escherichia coli* ATP synthase F1 sector: the epsilon subunit-sensitive rotation. *J Biol Chem* 281:4126-4131.
5. Omote, H., N. Sambonmatsu, K. Saito, Y. Sambongi, A. Iwamoto-Kihara, T. Yanagida, Y. Wada, and M. Futai. 1999. The gamma-subunit rotation and torque generation in F1-ATPase from wild-type or uncoupled mutant *Escherichia coli*. *Proc Natl Acad Sci U S A* 96:7780-7784.
6. Pilizota, T., T. Bilyard, F. Bai, M. Futai, H. Hosokawa, and R. M. Berry. 2007. A programmable optical angle clamp for rotary molecular motors. *Biophys J* 93:264-275.
7. Itoh, H., A. Takahashi, K. Adachi, H. Noji, R. Yasuda, M. Yoshida, and K. Kinosita. 2004. Mechanically driven ATP synthesis by F1-ATPase. *Nature* 427:465-468.
8. Hirono-Hara, Y., K. Ishizuka, K. Kinosita, Jr., M. Yoshida, and H. Noji. 2005. Activation of pausing F1 motor by external force. *Proc Natl Acad Sci U S A* 102:4288-4293.
9. Sowa, Y., B. C. Steel, R. M. Berry. 2010. A simple backscattering microscope for fast tracking of biological molecules. *Rev. Sci. Instrum.* 81, 113704.
10. Little, M.A., B. C. Steel, F. Bai, Y. Sowa, T. Bilyard, D. M. Mueller, R. M. Berry, N. S. Jones. 2011. Steps and bumps: precision extraction of discrete states of molecular machines. *Biophys J* 101:477-485
11. Thompson, R. E., D. R. Larson, W. W. Webb. 2002. Precise Nanometer Localization Analysis for Individual Fluorescent Probes. *Biophys J* 82:2775-2783.
12. Schwarz, G. 1978. Estimating the dimension of a model. *Ann Stats* 6:461-464.